ECOLE POLYTECHNIQUE
CENTRE DE MATHÉMATIQUES APPLIQUÉES

UMR CNRS 7641

91128 PALAISEAU CEDEX (FRANCE). Tel.: 01 69 33 46 00. Fax: 01 69 33 46 46
http : //www.cmap.polytechnique.fr/

Inversion of weighted Radon transforms via finite Fourier series weight approximations

J-P. Guillement, R.G. Novikov

R.I. 770 *February 2013*

Inversion of weighted Radon transforms via finite Fourier series weight approximations

J.-P. Guillement [1], **R.G. Novikov** [2]

[1] CNRS, Laboratoire de Mathématiques Jean Leray (UMR 6629), Université de Nantes, BP 92208, 44322, Nantes cedex 03, France
e-mail: guillement@math.univ-nantes.fr
[2] CNRS (UMR 7641), Centre de Mathématiques Appliquées, Ecole Polytechnique, 91128 Palaiseau, France
e-mail: novikov@cmap.polytechnique.fr

Abstract. We consider weighted Radon transforms on the plane. We show that the Chang approximate inversion formula for these transforms admits a principal refinement as inversion via finite Fourier series weight approximations. We illustrate this inversion approach by numerical examples for the case of the attenuated Radon transforms in the framework of the single-photon emission computed tomography (SPECT).

1. Introduction

A basic problem of many tomographies consists in finding an unknown function f on $\mathbb{R}^2$ from its weighted ray transform $P_W f$ on $\mathbb{R} \times \mathbb{S}^1$ for some known weight W, where

$$\begin{aligned} &P_W f(s,\theta) = \int\limits_{\mathbb{R}} W(s\theta^\perp + t\theta, \theta) f(s\theta^\perp + t\theta) dt, \\ &s \in \mathbb{R}, \quad \theta = (\theta_1, \theta_2) \in \mathbb{S}^1, \quad \theta^\perp = (-\theta_2, \theta_1), \end{aligned} \tag{1.1}$$

where $f = f(x)$, $W = W(x,\theta)$, $x \in \mathbb{R}^2$. Up to change of variables, the operator P_W is known also in the literature as the weighted Radon transform on the plane. In this work we always assume that

$$\begin{aligned} &W \in C(\mathbb{R}^2 \times \mathbb{S}^1) \cap L^\infty(\mathbb{R}^2 \times \mathbb{S}^1), \\ &w_0(x) \stackrel{\text{def}}{=} \frac{1}{2\pi} \int\limits_{\mathbb{S}^1} W(x,\theta) d\theta \neq 0, \quad x \in \mathbb{R}^2, \end{aligned} \tag{1.2}$$

where W is complex-valued, in general, and $d\theta$ is the standard element of arc length on $\mathbb{S}^1$. Additional assumptions on W will be formulated in the framework of context. In particular, in important particular cases W is real-valued and strictly positive:

$$W = \bar{W}, \quad W \geq c > 0. \tag{1.3}$$

In addition, for this work one can always assume that

$$f \in L^\infty(\mathbb{R}^2), \quad supp\, f \subset D, \tag{1.4}$$

where f is complex-valued, in general, and D is an open bounded domain (which is fixed a priori).

In definition (1.1) the product $\mathbb{R} \times \mathbb{S}^1$ is interpreted as the set of all oriented straight lines in $\mathbb{R}^2$. If $\gamma = (s, \theta) \in \mathbb{R} \times \mathbb{S}^1$, then $\gamma = \{x \in \mathbb{R}^2 : \ x = s\theta^\perp + t\theta, t \in \mathbb{R}\}$ (modulo orientation) and θ gives the orientation of γ.

If $W \equiv 1$, then P_W is reduced to the classical ray (or Radon) transform on the plane. If

$$W(x, \theta) = \exp\left(-\int\limits_0^{+\infty} a(x + t\theta)dt\right), \tag{1.5}$$

where a is a complex-valued sufficiently regular function on $\mathbb{R}^2$ with sufficient decay at infinity, then P_W is known in the literature as the attenuated ray (or Radon) transform on the plane.

The classical ray transform arises, in particular, in X-ray transmission tomography, see e.g. [Na]. The attenuated ray transform (at least, with real-valued $a \geq 0$) arises, in particular, in single-photon emission computed tomography (SPECT), see e.g. [Na], [Ku]. Transforms P_W with some other weights also arise in applications, see e.g. [Q], [Ku], [MP], [Ba].

Exact and simultaneously explicit inversion formulas for the classical and attenuated ray (or Radon) transforms on the plane were given for the first time in [Ra] and [No1], respectively. For some other weights W, exact and simultaneously explicit inversion formulas were given in [TM], [BS], [G], [No2]. Note that we say that an inversion method for P_W is an explicit inversion formula if its complexity is comparable with complexity of the aforementioned Radon inversion formula of [Ra].

Apparently, for general P_W, under assumptions (1.2), (1.3), explicit and simultaneously exact (modulo $Ker\, P_W$) inversion formulas are impossible. In addition, [Bo] gives an example of infinitely smooth W satisfying (1.2), (1.3) and such that $Ker\, P_W \neq 0$ in the space of infinitely smooth compactly supported functions on $\mathbb{R}^2$. But, due to [BQ], $Ker\, P_W = 0$ in the space of continuous compactly supported functions on $\mathbb{R}^2$ for real-analytic W satisfying (1.3).

On the other hand, the following Chang approximate (but explicit) inversion formula for P_W, where W is given by (1.5) with $a \geq 0$, has been used for a long time (see e.g. [Ch], [Ku], [No2]):

$$f_{appr} = (w_0)^{-1} P^{-1} P_W f, \tag{1.6}$$

where w_0 is defined in (1.2), P^{-1} denotes the classical Radon inversion realized via the formula

$$\begin{aligned} &P^{-1}q(x) = \frac{1}{4\pi}\int\limits_{\mathbb{S}^1} \theta^\perp \nabla_x \left(\frac{1}{\pi} p.v. \int\limits_{\mathbb{R}} \frac{q(t, \theta)}{x\theta^\perp - t} dt\right) d\theta, \quad x \in \mathbb{R}^2, \\ &\theta^\perp \nabla_x = -\theta_2 \partial/\partial x_1 + \theta_1 \partial/\partial x_2, \quad x\theta^\perp = -\theta_2 x_1 + \theta_1 x_2, \quad \theta = (\theta_1, \theta_2), \quad x = (x_1, x_2), \end{aligned} \tag{1.7}$$

where q is a test function on $\mathbb{R} \times \mathbb{S}^1$. It is known that formula (1.6) is efficient for the first approximation in SPECT reconstructions and, in particular, is sufficiently stable for reconstructions from discrete data with strong Poisson noise. The exact inversion formula

of [No1] for the attenuated ray transform is considerably less stable in this respect. For more information in this connection see [GN2].

Formula (1.6), under assumptions (1.2), can be considered as approximate inversion of P_W via the approximation

$$W(x,\theta) \approx w_0(x), \quad x \in \mathbb{R}^2, \quad \theta \in \mathbb{S}^1, \tag{1.8}$$

i.e. via the zero term Fourier approximation for W in angle variable. In addition, due to [Ra], formula (1.5) is exact if

$$W(x,\theta) \equiv w_0(x), \quad x \in \mathbb{R}^2, \quad \theta \in \mathbb{S}^1. \tag{1.9}$$

Besides, due to [No2], formula (1.5) is exact if and only if

$$W(x,\theta) - w_0(x) \equiv w_0(x) - W(x,-\theta), \quad x \in \mathbb{R}^2, \quad \theta \in \mathbb{S}^1. \tag{1.10}$$

However, already for W of (1.5) property (1.10) is not fulfilled, in general.

In the present work we consider approximate inversion of P_W via the approximations

$$\begin{aligned} &W(x,\theta(\varphi)) \approx \sum_{n=-N}^{N} e^{in\varphi} w_n(x), \\ &w_n(x) = \frac{1}{2\pi} \int_{-\pi}^{\pi} e^{-in\varphi} W(x,\theta(\varphi)) d\varphi, \\ &x \in \mathbb{R}^2, \ \theta(\varphi) = (\cos\varphi, \sin\varphi), \quad \varphi \in [-\pi,\pi], \quad N \in \mathbb{N} \cup 0. \end{aligned} \tag{1.11}$$

One can see that for $N = 0$ approximation (1.11) is reduced to (1.8).

Our approximate inversion algorithms for P_W on functions of (1.4), under assumptions (1.2), are presented in Subsection 2.4 of Section 2. In these considerations we proceed from [Ku] and [No3].

In Section 3, our approximate inversions (2.20), (2.22) of Subsection 2.4 are illustrated by numerical examples for W given by (1.5) with $a \geq 0$ in the framework of SPECT.

2. Approximate inversion of P_W

2.1. Symmetrization of W. Let

$$A_W f = P^{-1} P_W f, \tag{2.1}$$

where P^{-1} is defined by (1.7). Let

$$W_{sym}(x,\theta) = \frac{1}{2}(W(x,\theta) + W(x,-\theta)), \quad x \in \mathbb{R}^2, \quad \theta \in \mathbb{S}^1. \tag{2.2}$$

We consider also the Fourier series

$$W(x,\theta(\varphi)) = \sum_{n=-\infty}^{+\infty} e^{in\varphi} w_n(x), \quad x \in \mathbb{R}^2, \quad \varphi \in [-\pi,\pi], \tag{2.3}$$

where w_n are defined in (1.11), $\theta(\varphi) = (\cos\varphi, \sin\varphi)$.

The following formulas hold (see [Ku], [No2]):

$$\frac{1}{2}\Big(P_W f(s,\theta) + P_W f(-s,-\theta)\Big) = P_{W_{sym}} f(s,\theta), \quad (s,\theta) \in \mathbb{R}\times\mathbb{S}^1, \tag{2.4}$$

$$A_W f = P^{-1} P_{W_{sym}} f, \tag{2.5}$$

$$W_{sym}(x,\theta(\varphi)) = \sum_{l=-\infty}^{+\infty} e^{i2l\varphi} w_{2l}(x), \quad x \in \mathbb{R}^2, \quad \varphi \in [-\pi,\pi]. \tag{2.6}$$

Actually, using (2.4)-(2.6) we reduce inversion of P_W to inversion of $P_{W_{sym}}$. In particular, using (2.1), (2.5), (2.6), one can see that such a reduction arises already in the framework of (1.6).

2.2. Operators $Q_{W,D,m}$ and numbers $\sigma_{W,D,m}$. Consider

$$z = x_1 + ix_2, \quad \bar{z} = x_1 - ix_2, \quad x = (x_1, x_2) \in \mathbb{R}^2. \tag{2.7}$$

Using (2.7) we identify $\mathbb{R}^2$ with $\mathbb{C}$.

Let Π, $\bar{\Pi}$ denote the linear integral operators on $\mathbb{R}^2$ identified with $\mathbb{C}$ such that

$$\begin{aligned} \Pi u(z) &= -\frac{1}{\pi}\int\limits_{\mathbb{C}} \frac{u(\zeta)}{(\zeta - z)^2} dRe\,\zeta\; dIm\,\zeta, \\ \bar{\Pi} u(z) &= -\frac{1}{\pi}\int\limits_{\mathbb{C}} \frac{u(\zeta)}{(\bar{\zeta} - \bar{z})^2} dRe\,\zeta\; dIm\,\zeta, \end{aligned} \tag{2.8}$$

where u is a test function, $z \in \mathbb{C}$; see e.g. [V] for detailed properties of these operators.

Let D be the domain of (1.4).

Let χ_D denote the characteristic function of D, i.e.

$$\chi_D \equiv 1 \ \text{ on } \ D, \quad \chi_D \equiv 0 \ \text{ on } \ \mathbb{R}^2 \backslash D. \tag{2.9}$$

Let

$$\begin{aligned} &Q_{W,D,m} = \sum_{l=1}^{m} \left((-\bar{\Pi})^l \frac{w_{2l}}{w_0} + (-\Pi)^l \frac{w_{-2l}}{w_0} \right) \chi_D \ \text{ for } \ m \in \mathbb{N}, \\ &Q_{W,D,m} = 0 \ \text{ for } \ m = 0, \end{aligned} \tag{2.10}$$

where w_0, w_{2l} are the Fourier coefficients of (2.3), (2.6) and $w_{\pm 2l}/w_0$, χ_D are considered as the multiplication operators on $\mathbb{R}^2$.

Let

$$\begin{aligned} &\sigma_{W,D,m} = \sum_{l=1}^{m} \left(\sup_{x\in D} \left| \frac{w_{2l}(x)}{w_0(x)} \right| + \sup_{x\in D} \left| \frac{w_{-2l}(x)}{w_0(x)} \right| \right) \ \text{ for } \ m \in \mathbb{N}, \\ &\sigma_{W,D,m} = 0 \ \text{ for } \ m = 0. \end{aligned} \tag{2.11}$$

According to [No3] we have that

$$\|Q_{W,D,m}\|_{L^2(\mathbb{R}^2)\to L^2(\mathbb{R}^2)} \le \sigma_{W,D,m}. \tag{2.12}$$

2.3. Exact inversion for finite Fourier series weights. Let conditions (1.2), (1.4) be fulfilled and

$$\begin{aligned} &W(x,\theta(\varphi)) = \sum_{n=-N}^{N} e^{in\varphi} w_n(x), \\ &x \in \mathbb{R}^2, \quad \theta(\varphi) = (\cos\varphi, \sin\varphi), \quad \varphi \in [-\pi,\pi], \quad N \in \mathbb{N} \cup 0. \end{aligned} \tag{2.13}$$

Suppose also that

$$\sigma_{W,D,m} < 1 \ \text{ for } \ m = [N/2], \tag{2.14}$$

where $[N/2]$ denotes the integer part of $N/2$. Then according to [No3] we have the following exact inversion for P_W:

$$f = (w_0)^{-1}(I + Q_{W,D,m})^{-1} P^{-1} P_W f, \tag{2.15}$$

where I is the identity operator on $\mathbb{R}^2$, P^{-1} is defined by (1.7). In addition, in view of (2.12), (2.14) we have that

$$(I + Q_{W,D,m})^{-1} = I + \sum_{j=1}^{+\infty} (-Q_{W,D,m})^j. \tag{2.16}$$

In addition, under our assumptions, we have that (see [No3]):

$$A_W f = P^{-1} P_W f \in L^2(\mathbb{R}^2). \tag{2.17}$$

2.4. Approximate inversion for general weights. Let conditions (1.2), (1.4) be fulfilled and

$$\sum_{l=1}^{\infty} \left(\left\| \frac{w_{2l}}{w_0} \right\|_{L^2(D)} + \left\| \frac{w_{-2l}}{w_0} \right\|_{L^2(D)} \right) < +\infty, \tag{2.18}$$

where w_n are defined by (2.11). Suppose that

$$\sigma_{W,D,m} < 1 \ \text{ for fixed } \ m \in \mathbb{N} \cup 0. \tag{2.19}$$

Then we consider that

$$f \approx f_m, \tag{2.20a}$$

$$f_m = (w_0)^{-1}(I + Q_{W,D,m})^{-1} P^{-1} P_W f, \tag{2.20b}$$

where I is the identity operator, $Q_{W,D,m}$ is defined by (2.10), P^{-1} is defined by (1.7). Note that the right-hand side of (2.20b) is well-defined: in particular, in view of (2.12), (2.19) we have formula (2.16) in norm $\|\cdot\|_{L^2(\mathbb{R}^2)\to L^2(\mathbb{R}^2)}$ and using (2.18) one can show that

$$P^{-1}P_W f \in L^2(\mathbb{R}^2). \tag{2.21}$$

Formula (2.20) is a natural extension of the Chang formula (1.6). In particular, (2.20) for $m = 0$ coincides with (1.6).

In addition, if (2.19) is fulfilled for some $m \geq 1$, then f_m is a refinement of the Chang approximation f_0 and, more generally, f_j is a refinement of f_i for $0 \leq i < j \leq m$. But of course $f_j = f_i$ if $w_{2l} \equiv 0$, $w_{-2l} \equiv 0$ for $i < l \leq j$.

Actually, in many important examples condition (2.19) is efficiently fulfilled for small m (e.g. $m = 2$) and is not fulfilled for great m. Therefore, in the present work we propose the following approximate reconstruction of f from $P_W f$:

$$\begin{aligned}&\text{find maximal } \ m \ \text{ such that } \ (2.19) \ \text{ is still efficiently fulfilled}\\ &\text{and approximately reconstruct } \ f \ \text{ via } (2.20) \ \text{ using } (2.12), (2.16).\end{aligned} \tag{2.22}$$

In Section 3 we illustrate this approximate reconstruction by numerical examples in the framework of SPECT. In particular, these numerical examples show that stability properties of this approximate reconstruction f_m are similar to stability properties of the Chang approximate reconstruction f_0 but f_m is more precise than f_0 if $m > 0$.

Using considerations of Subsection 2.3 one can see also that

$$f = f_m - (w_0)^{-1}(I + Q_{W,D,m})^{-1}P^{-1}P_{\delta W_m} f, \tag{2.23}$$

where

$$\delta W_m(x, \theta(\varphi)) \stackrel{\text{def}}{=} W(x, \theta(\varphi)) - \sum_{n=-2m-1}^{2m+1} e^{in\varphi} w_n(x), \tag{2.23}$$

$$x \in \mathbb{R}^2, \quad \theta(\varphi) = (\cos\varphi, \sin\varphi), \quad \varphi \in [-\pi, \pi], \quad m \in \mathbb{N} \cup 0, \tag{2.24}$$

where w_n are defined by (1.11). One can use (2.23) for estimating the error $f - f_m$. One can also consider (2.23) as an integral equation for finding f from f_m. Note also that equation (2.23) for $m = 0$ is, actually, well-known, see e.g. [Ku].

2.5. Relations with [Ku]. Let conditions (1.2), (1.4) be fulfilled and

$$\lim_{m\to+\infty} \sigma_{W,D,m} = \sigma_{W,D} < +\infty. \tag{2.25}$$

Then we can consider

$$Q_{W,D} = \lim_{m\to+\infty} Q_{W,D,m} \ \text{ in } \ \|\cdot\|_{L^2(\mathbb{R}^2)\to L^2(\mathbb{R}^2)}. \tag{2.26}$$

In addition, if

$$\sigma_{W,D} < 1, \tag{2.27}$$

then

$$f = (w_0)^{-1}(I + Q_{W,D})^{-1}P^{-1}P_W f, \tag{2.28}$$

$$(I + Q_{W,D})^{-1} = I + \sum_{j=1}^{+\infty}(-Q_{W,D})^j. \tag{2.29}$$

Actually, (2.28) is a linear integral equation for exact reconstruction of f from $P_W f$ under assumptions (1.2), (1.4), (2.27). In addition, (2.29) can be interpreted as the method of successive approximations for solving this equation.

It is possible to show that the reconstruction of f from $P_W f$ of [Ku] (or, more precisely, the linear integral equation on ε on page 814 of [Ku]) can be transformed into (2.28).

In [Ku] (under the assumption that $0 < W < 1$) it was shown that this equation on ε of [Ku] is uniquely solvable if

$$\begin{gathered}\lim_{m\to+\infty}\rho_{W,D,m} = \rho_{W,D} < 1,\\ \rho_{W,D,m} \stackrel{\text{def}}{=} \frac{\sum_{l=1}^{m}(\sup\limits_{x\in D}|w_{2l}(x)| + \sup\limits_{x\in D}|w_{-2l}(x)|)}{\min\limits_{x\in D}|w_0(x)|}.\end{gathered} \tag{2.30}$$

One can see that in many cases $\sigma_{W,D,m}$ is much smaller than $\rho_{W,D,m}$ and condition (2.27) is much less restrictive than (2.30).

Actually, in order to relate considerations of [Ku] on one hand with considerations of [No3] and the present work on the other hand, we use the following formulas

$$\begin{aligned}&\mathcal{F}(\Pi^l u)(\xi) = \left(\frac{\xi_1 - i\xi_2}{\xi_1 + i\xi_2}\right)^l \mathcal{F}u(\xi),\\ &\mathcal{F}(\bar{\Pi}^l u)(\xi) = \left(\frac{\xi_1 + i\xi_2}{\xi_1 - i\xi_2}\right)^l \mathcal{F}u(\xi),\\ &\xi = (\xi_1, \xi_2) \in \mathbb{R}^2, \quad l \in \mathbb{N},\end{aligned} \tag{2.31}$$

$$\begin{aligned}&Q_{W,D,m}u(x) = P^{-1}(P_{W,D,m}u)(x),\\ &P_{W,D,m}u(s,\theta) \stackrel{\text{def}}{=} \int\limits_{\mathbb{R}}\left(\left(\sum_{l=-m}^{-1} + \sum_{l=1}^{m}\right)\frac{w_{2l}(s\theta^\perp + t\theta)}{w_0(s\theta^\perp + t\theta)}(\theta_1 + i\theta_2)^{2l}\right)\times\\ &\chi_D(s\theta^\perp + t\theta)u(s\theta^\perp + t\theta)dt,\\ &x \in \mathbb{R}^2, \quad s \in \mathbb{R}, \quad \theta = (\theta_1, \theta_2) \in \mathbb{S}^1, \quad m \in \mathbb{N},\end{aligned} \tag{2.32}$$

where $\mathcal{F}$ denotes the $2D$ Fourier transform operator, Π, $\bar{\Pi}$ are defined by (2.8), Q_m is defined by (2.10), P^{-1} is defined by (1.7), u is a test function.

Finally, note that in our numerical examples of Section 3 the approximate reconstruction (2.20) is realized numerically using formula (2.32).

3. Numerical examples

3.1. Framework of SPECT. All numerical examples of this work are given in the framework of SPECT. In particular, we assume that W is given by (1.5), where $a \geq 0$. We recall that in SPECT, after restricting the problem to a fixed $2D$ plane, the functions $P_W f$, a, f are interpreted as follows:

- f is distribution of radioactive isotopes emitting photons;
- a is photon attenuation coefficient;
- in addition, it is assumed that $supp\, a \subseteq D$, $supp\, f \subseteq D$, where D is some known compact domain;
- $P_W f$ describes the expected radiation outside D.

In addition, in some approximation, measured SPECT data are modeled as $P_W f$ with Poisson noise on some discrete subset Γ of $\mathbb{R} \times \mathbb{S}^1$. Usually, it is also assumed that:

- $D \subset \mathcal{B}_R = \{x \in \mathbb{R}^2 : \ |x| \leq R\}$, where R is the radius of image support,
- Γ is a uniform $n \times n$ sampling of

$$T_R = \{\gamma \in \mathbb{R} \times \mathbb{S}^1 : \ \gamma \cap \mathcal{B}_R \neq 0\} = \{(s, \theta) \in \mathbb{R} \times \mathbb{S}^1 : \ |s| \leq R\}. \tag{3.1}$$

For more information on SPECT see e.g. [Na], [Br], [GN1] and references therein.

3.2. Image parameters. All $2D$ images of this work are considered on $n \times n$ grids (X and Γ), where $n = 128$. We assume that X is a uniform $n \times n$ sampling of

$$\mathcal{D}_R = \{x = (x_1, x_2) \in \mathbb{R}^2 : \ |x_1| \leq R, \ \ |x_2| \leq R\} \tag{3.2}$$

and Γ is a uniform $n \times n$ sampling of T_R, where R is the radius of the image support.

In addition, all $2D$ images of this work are drawn using a linear greyscale in such a way that the dark grey color represents zero (or negative values, if any) and white corresponds to the maximum value of the imaged function.

3.3. Numerical phantoms. We consider two numerical phantoms (phantom 1 and phantom 2). Attenuation maps a, emitter activities f, noiseless emission data $g = P_W f$ and noisy emission data p for these phantoms are shown in figures 1 and 2.

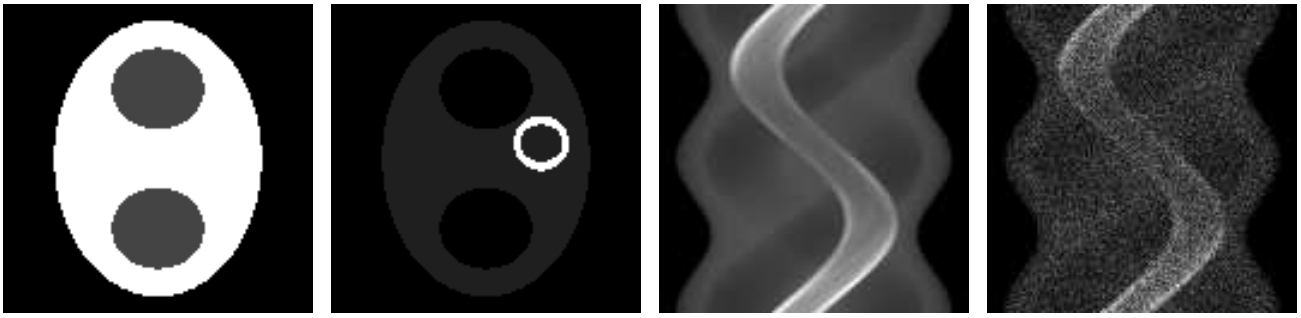

(a) (b) (c) (d)

Figure 1. Attenuation map a (a), emitter activity f (b), noiseless emission data $g = P_W f$ (c), noisy emission data p (d) for phantom 1. (See Subsections 3.1, 3.3)

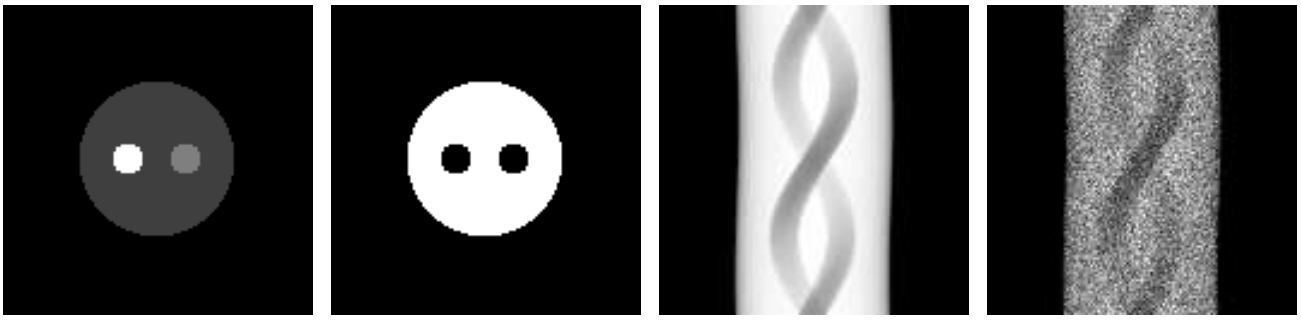

(a) (b) (c) (d)

Figure 2. Attenuation map a (a), emitter activity f (b), noiseless emission data $g = P_W f$ (c), noisy emission data p (d) for phantom 2. (See Subsections 3.1, 3.3)

Phantom 1 is a version of the elliptical chest phantom (used for numerical simulations of cardiac SPECT imaging; see e.g. [Br], [GN1], [GN2]). Actually, this version is the same as in [GN1], [GN2] and, in addition to figure 1, its description includes the following information:

• the major axis of the ellipse representing the body is 30 cm,

• attenuation coefficient a is 0.04 cm^{-1} in the lung region (modeled as two interior ellipses), 0.15 cm^{-1} elsewhere within the body ellipse, and zero outside the body,

• emitter activity f is in the ratio 8:0:1:0 in myocardium (represented as a ring), lungs, elsewhere within the body, and outside the body,

• noisy emission data p contain 30 percents of the Poisson noise in the sense of L^2-norm and the total number of photons is 125 450.

Phantom 2 is a simulated numerical version of the Utah phantom (designed at the 2^{nd} International Meeting on fully Three-Dimensional Image Reconstruction in Radiology and Nuclear Medicine, Snowbird, Utah, 1993). A real non simulated version of this phantom was considered, in particular, in [GJKNT]. However, in the present work we consider its simulated numerical version in order to see clearly different reconstruction errors. In addition to figure 2, the description of phantom 2 includes the following information:

• geometrically the phantom consists of a large disk containing two small disks, where the radius of the large disks 10 cm,

• attenuation coefficient a is 0.16 cm^{-1} in the large disk outside the small disks, 0.63 cm^{-1} in the left small disk, 0.31 cm^{-1} in the right small disk, and zero outside the large disk,
• emitter activity f is a positive constant in the large disk outside the small disks and zero elsewhere
• noisy emission data p contain 30 percents of the Poisson noise in the sense of L^2-norm and the total number of photons is 89 350.

Note also that all computations of the present work are fulfilled using the same numerical realizations of basic formulas as in [GJKNT], [GN1], [GN2].

3.4. Results for the bounds $\sigma_{W,D,m}$ and $\rho_{W,D,m}$. The bound numbers $\sigma_{W,D,m}$, $\rho_{W,D,m}$ of (2.11), (2.30) for phantoms 1 and 2 are shown in tables 1 and 2, where $D = \mathcal{B}_R$.

Table 1. Numbers $\sigma_{W,D,m}$, $\rho_{W,D,m}$ of (2.11), (2.30) for phantom 1, where $D = \mathcal{B}_R$.

	$m=1$ |	$m=2$ |	$m=3$ |	$m=20$ |
$\sigma_{W,D,m}$ |	0.390 |	0.584 |	0.739 |	1.320 |
$\rho_{W,D,m}$ |	1.399 |	2.025 |	2.494 |	4.532 |

Table 2. Numbers $\sigma_{W,D,m}$, $\rho_{W,D,m}$ of (2.11), (2.30) for phantom 2, where $D = \mathcal{B}_R$.

	$m=1$ |	$m=2$ |	$m=3$ |	$m=20$ |
$\sigma_{W,D,m}$ |	0.489 |	0.694 |	0.803 |	1.296 |
$\rho_{W,D,m}$ |	3.112 |	4.567 |	5.436 |	9.719 |

For phantoms 1 and 2, tables 1 and 2 show that condition (2.19) is efficiently fulfilled, at least, for $m = 1$ and $m = 2$, whereas $\rho_{W,D,m} > 1$ already for $m = 1$.

3.5. Reconstruction results. For phantoms 1 and 2 we consider the approximate reconstructions f_m realized numerically via (2.20b) (using the method of successive approximations i.e. using (2.16)) from the noiseless data g and filtered noisy data $\tilde{p}$. In addition:

• we consider f_m, mainly, under the condition that $\sigma_{W,D,m} \leq 0.7$,

• we consider $\tilde{p} = \mathcal{W}p$ for $\mathcal{W} = \mathcal{A}^{sym}_{8,8}$, where $\mathcal{W} = \mathcal{A}^{sym}_{l_1,l_2}$ is the approximately optimal space-variant Wiener-type filter of Section 5.3 of [GN1].

In addition to f_m we consider also their non-negative parts f^+_m, where

$$f^+_m(x) = f_m(x) \text{ if } f_m(x) \geq 0 \text{ and } f^+_m(x) = 0 \text{ if } f_m(x) < 0$$

For phantoms 1 and 2, tables 1 and 2 show that $\sigma_{W,D,m} \leq 0.7$ is fulfilled for $m = 0, 1, 2$ only.

To study reconstruction errors we consider, in particular,

$$\eta(u_2, u_1, X) = \frac{\|u_2 - u_1\|_{L^2(X)}}{\|u_1\|_{L^2(X)}}, \tag{3.3}$$

where u_1, u_2 are test functions on X.

The approximate reconstructions f_0, f_2 with their central horizontal profiles from the noiseless data g for phantoms 1 and 2 are shown in figures 3 and 4.

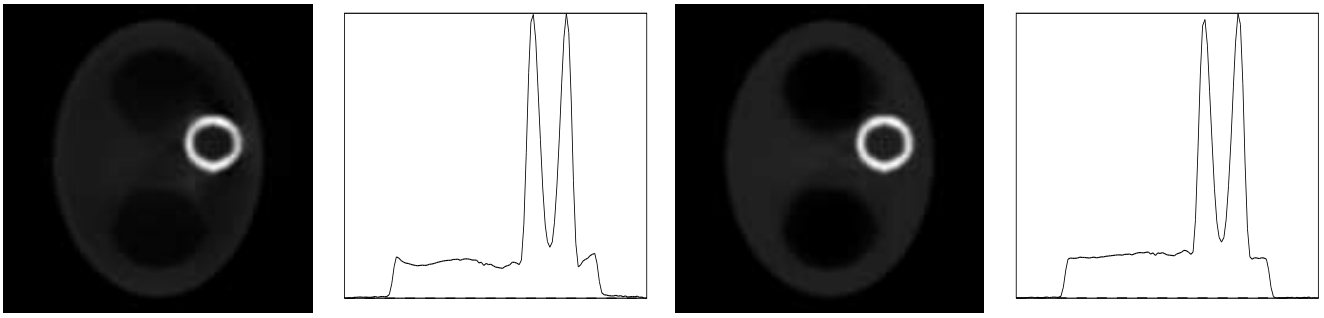

(a) (b) (c) (d)

Figure 3. Approximate reconstructions f_0 (a) and f_2 (c) with their central horizontal profiles (b) and (d) from the noiseless data g for phantom 1. (See Subsections 3.3, 3.5)

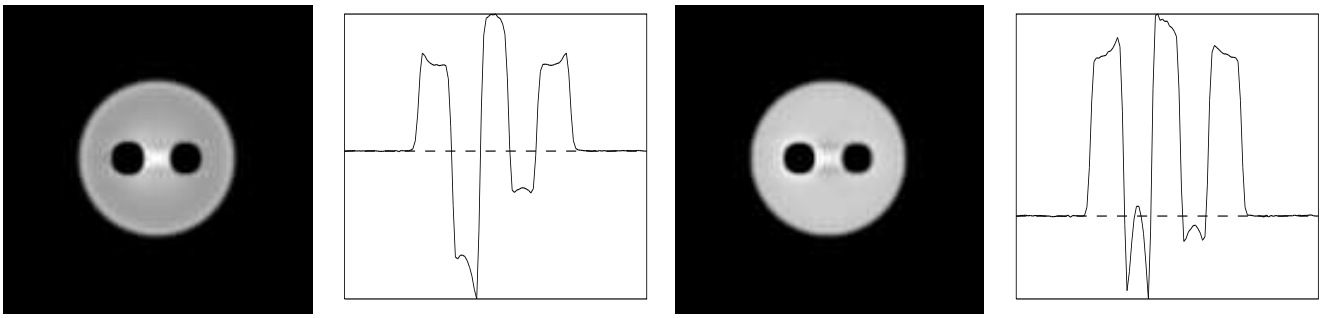

(a) (b) (c) (d)

Figure 4. Approximate reconstructions f_0 (a) and f_2 (c) with their central horizontal profiles (b) and (d) from the noiseless data g for phantom 2. (See Subsections 3.3, 3.5)

Tables 3 and 4 show the relative errors $\eta(f_m, f, X)$ and $\eta(f_m^+, f, X)$ in L^2- norm for the approximate reconstructions f_m with respect to precise f for the noiseless case for phantoms 1 and 2.

Table 3. Relative reconstruction errors $\eta(f_m, f, X),\ \eta(f_m^+, f, X)$ for the noiseless case for phantom 1.

	$m=0$ |	$m=1$ |	$m=2$ |	$m=3$ |
$\eta(f_m, f, X)$ |	0.331 |	0.305 |	0.295 |	0.295 |
$\eta(f_m^+, f, X)$ |	0.331 |	0.305 |	0.295 |	0.293 |

Table 4. Relative reconstruction errors $\eta(f_m, f, X),\ \eta(f_m^+, f, X)$ for the noiseless case for phantom 2.

	$m=0$ |	$m=1$ |	$m=2$ |	$m=3$ |
$\eta(f_m, f, X)$ |	0.292 |	0.179 |	0.152 |	0.141 |
$\eta(f_m^+, f, X)$ |	0.168 |	0.151 |	0.138 |	0.136 |

Figures 3, 4 and tables 3, 4 show that for phantoms 1 and 2 for the noiseless case the approximations f_1, f_2 are considerably more precise than the classical Chang approximation f_0.

The approximate reconstructions f_0, f_2 with their central horizontal profiles from the filtered noisy data $\tilde{p} = \mathcal{A}^{sym}_{8,8} p$ for phantoms 1 and 2 are shown in figures 5 and 6, where $\mathcal{A}^{sym}_{l_1,l_2}$ is the aforementioned filter of [GN1].

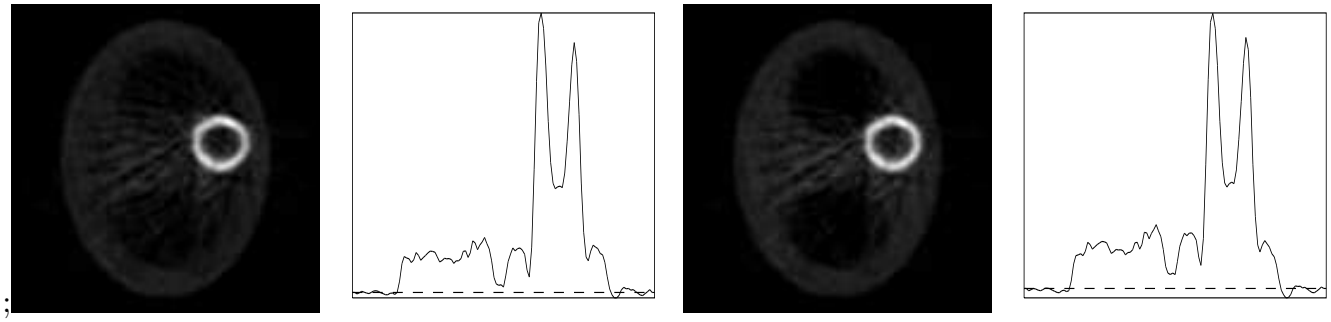

(a) (b) (c) (d)

Figure 5. Approximate reconstructions f_0 (a) and f_2 (c) with their central horizontal profiles (b) and (d) from the filtered noisy data $\tilde{p} = \mathcal{A}^{sym}_{8,8} p$ for phantom 1.

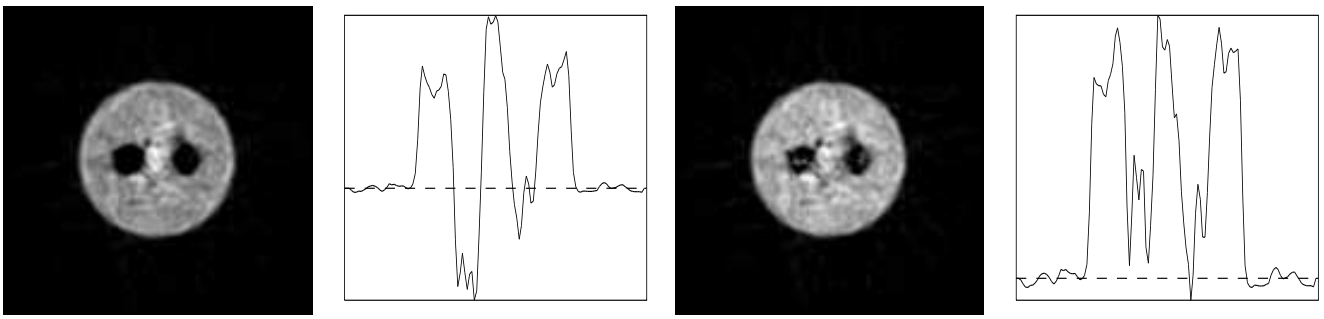

(a) (b) (c) (d)

Figure 6. Approximate reconstructions f_0 (a) and f_2 (c) with their central horizontal profiles (b) and (d) from the filtered noisy data $\tilde{p} = \mathcal{A}^{sym}_{8,8} p$ for phantom 2.

Tables 5 and 6 show the relative errors $\eta(f_m, f, X)$ and $\eta(f_m^+, f, X)$ in L^2- norm for f_m reconstructed from filtered noisy data $\tilde{p} = \mathcal{A}^{sym}_{8,8} p$ for phantoms 1 and 2.

Table 5. Relative errors $\eta(f_m, f, X)$, $\eta(f_m^+, f, X)$ for f_m reconstructed from $\tilde{p} = \mathcal{A}^{sym}_{8,8} p$ for phantom 1.

	$m=0$|	$m=1$|	$m=2$|	$m=3$|
$\eta(f_m, f, X)$ |	0.398 |	0.380 |	0.374 |	0.373 |
$\eta(f_m^+, f, X)$ |	0.398 |	0.379 |	0.373 |	0.371 |

Table 6. Relative errors $\eta(f_m, f, X)$, $\eta(f_m^+, f, X)$ for f_m reconstructed from $\tilde{p} = \mathcal{A}^{sym}_{8,8} p$ for phantom 2.

	$m=0$|	$m=1$|	$m=2$|	$m=3$|
$\eta(f_m, f, X)$ |	0.268 |	0.218 |	0.218 |	0.225 |
$\eta(f_m^+, f, X)$ |	0.214 |	0.209 |	0.213 |	0.221 |

Figures 5, 6 and tables 5, 6 show that for phantoms 1 and 2 for the noisy case the approximations f_1, f_2 are also more correct than the classical Chang approximation f_0.

4. Conclusions

In this work we showed that the classical Chang approximate inversion formula (1.6) admits a very natural extention into inversion via finite Fourier series weight approximations or, more precisely, into inversion via (2.20) considered under assumption (2.19). Related theoretical considerations are presented in Sections 1 and 2 and numerical examples in the framework of SPECT are given in Section 3. Our examples of Section 3 include comparisons with the approximate Chang reconstruction f_0 and show numerical efficiency (with respect to precision and stability) of our approximate reconstructions f_m for $m > 0$, under the condition that inequality (2.19) is efficiently fulfilled.

Note also that considerations of Subsections 2.5 and 3.4 explain convergence of the iterative inversion of [Ku] for many cases when the inequality of (2.30) is not fulfilled. The point is that less restrictive inequality (2.27) is sufficient for this convergence.

References

[Ba] G. Bal, Inverse transport theory and applications, *Inverse Problems* **25** (2009), 053001 (48pp)

[Bo] J. Boman, An example of non-uniqueness for a generalized Radon transform, *J. Anal. Math.* **61** (1993), 395-401

[BQ] J. Boman and E.T. Quinto, Support theorems for real-analytic Radon transforms, *Duke Math. J.* **55** (1987), 943-948

[BS] J. Boman and J.O. Strömberg, Novikov's inversion formula for the attenuated Radon transform - a new approach, *J.Geom.Anal.* **14** (2004), 185-198

[Br] A.V. Bronnikov, Reconstruction of the attenuation map using discrete consistency conditions, IEEE Trans. Med. Imaging **19** (2000), 451-462

[Ch] L.T. Chang, A method for attenuation correction in radionuclide computed tomography, *IEEE Trans. Nucl. Sci.* NS-25 (1978), 638-643

[G] S. Gindikin, A remark on the weighted Radon transform on the plane, *Inverse Problems and Imaging* **4** (2010), 649-653

[GJKNT] J.-P. Guillement, F. Jauberteau, L. Kunyansky, R. Novikov and R. Trebossen, On single-photon emission computed tomography imaging based on an exact formula for the nonuniform attenuation correction, Inverse Problems **18** (2002), L11-L19

[GN1] J.-P. Guillement and R.G. Novikov, On Wiener type filters in SPECT, Inverse Problems **24** (2008), 025001

[GN2] J.-P. Guillement and R.G. Novikov, Optimized analytic reconstruction for SPECT, *J. Inv. Ill-Posed Problems*, **20** (2012), 489-500

[Ku] L.A. Kunyansky, Generalized and attenuated Radon transforms: restorative approach to the numerical inversion, *Inverse Problems* **8** (1992), 809-819

[MP] E.X. Miqueles and A.R. De Pierro, Fluorescence tomography: reconstruction by iterative methods, *ISBI* (2008), 760-763

[Na] F. Natterer, *The Mathematics of Computerized Tomography* (Stuttgart: Teubner), 1986

[No1] R.G. Novikov, An inversion formula for the attenuated X-ray transformation, *Ark. Mat.* **40** (2002), 145-167

[No2] R.G. Novikov, Weighted Radon transforms for which Chang's approximate inversion formula is exact, *Uspekhi Mat. Nauk* **66** (2) (2011), 237-238

[No3] R.G. Novikov, Weighted Radon transforms and first order differential systems on the plane, e-print: http://hal.archives-ouvertes.fr/hal-00714524

[Q] E.T. Quinto, The invertibility of rotation invariant Radon transforms, *J. Math. Anal. Appl.* **91** (1983), 510-522

[Ra] J. Radon, Uber die Bestimmung von Funktionen durch ihre Integralwerte langs gewisser Mannigfaltigkeiten, *Ber. Verh. Sachs. Akad. Wiss. Leipzig, Math-Nat.*, **K** 1 **69** (1917), 262-267

[TM] O.J. Tretiak and C. Metz, The exponential Radon transform, *SIAM J. Appl. Math.* **39** (1980), 341-354

[V] I.N. Vekua, *Generalized Analytic Functions*, Pergamon Press Ltd. 1962